Structural and Chemical Evolution of Highly Fluorinated Li-rich Disordered Rocksalt Oxyfluorides as a Function of Temperature

*Neelam Sunariwal, Fulya Dogan, Indrani Roy, Khagesh Kumar, Dennis Nordlund, Qing Ma, and Jordi Cabana**

N. Sunariwal, I. Roy, K. Kumar, J. Cabana

Department of Chemistry

University of Illinois at Chicago

Chicago, IL 60607, USA

E-mail: jcabana@uic.edu

F. Dogan

Chemical Sciences and Engineering Division

Argonne National Laboratory

Lemont, IL 60439, USA

D. Nordlund

Stanford Synchrotron Radiation Lightsource

SLAC National Accelerator Laboratory

Menlo Park, CA 94025, USA

Q. Ma

DND-CAT

Synchrotron Research Center

Northwestern University

Evanston, IL 60208, USA

Keywords

Lithium-ion batteries, lithium-rich disordered rocksalt oxyfluorides, structural ordering, X-ray absorption spectroscopy, electrochemical profiles.

Abstract:

Li-rich disordered rocksalt (DRS) oxyfluorides have emerged as promising high-energy cathode materials for lithium-ion batteries. While a high level of fluorination in DRS materials offers performance advantages, it can only be achieved *via* mechanochemical synthesis, which poses challenges of reproducibility and scalability. The definition of relationships between fluorination and structural stability is required to devise alternative methods that overcome these challenges. In this study, we investigated the thermal evolution of three highly fluorinated phases, Li_2TMO_2F (TM=Mn, Co, and Ni), in inert atmosphere. We utilized diffraction and spectroscopic techniques to examine their electronic and chemical states up until conditions of decomposition. The analysis revealed that the materials phase-separate above 400°C, at most. We also observed that heat-treated DRS materials exhibited intricate changes in local coordination of the metals, including their spin, and ordering compared to the pristine states. The changes upon annealing were accompanied by a modulation of the voltage profile, including reduced hysteresis, when used as electrodes. These results provide an in-depth understanding of the fundamental crystal chemistry of DRS oxyfluorides in view of their promising role as the next generation of Li-ion cathodes.

1. Introduction:

Rechargeable lithium-ion batteries are energy storage devices that have been used in a wide variety of applications.[1,2] Nonetheless, demand for high energy density cathode materials that can provide better discharge capacity, longer cycle life, and structural stability continues to exist.[3–5] Li-rich disordered rock salt (DRS) oxyfluorides are a recently discovered class of cathode materials that have garnered attention through their compositional versatility compared to layered oxides and their highly reversible discharge capacity.[6–8] These materials hold promise for use in future batteries with high energy density.[9] In a DRS phase, Li and transition metal (TM) are crystallographically mixed in the cationic sites of the rock salt structure.[10–13] When both O and F are present, they are also disordered in the anionic sites. The presence of F has shown to potentially stabilize the structure and surface chemistry of the DRS cathode materials during cycling.[14–16] Despite extensive research on the electrochemical performance of DRS oxyfluoride materials, very little is known about their stability, especially when a substantial amount of F is present.[17,18]

Li-rich DRS oxyfluorides cannot be synthesized via solid-state methods, the most desirable for their scalability and simplicity, if the F content is more than 10% of the total anions.[11] Higher fluorination levels of 33% or more can be achieved *via* mechanochemistry.[9,19] Nevertheless, ballmilling introduces challenges of scalability, partly due to issues with reproducibility associated with poor control of local structural distortions and defects. The contrast between solid-state and mechanochemical methods indicates that high fluorination levels are metastable. Establishing the precise stability of these cationic-anionic disordered arrangements is important to devise novel recipes of synthesis different from ballmilling and determine whether the cationic and anionic arrangements can be tuned for improved performance. Given the sensitivity of the specific profile

of the electrochemical response of a solid to the chemical potential of Li in its structure, it is reasonable to hypothesize that even small structural rearrangements would manifest in changes in the performance measurements conventionally conducted at constant current in the literature.[20]

The choice of atmosphere for heat-treatment can significantly influence the behavior of materials. In principle, inert atmosphere promotes phase separation into simpler components during heat-treatment, in contrast with atmospheres with O_2 or H_2, where oxidation or reduction will become more favorable. A study by Wang et al. investigated the thermal stability of Li_2VO_2F under N_2 flow and found it to decompose into LiF and ternary oxides ($LiVO_2$, Li_3VO_4 and $Li_{1.5}V_2O_4$) starting above 400°C.[17] The properties of disordered phases at temperatures just below decomposition was not established. Kanno et al. reported that Li_2MnO_2F decomposed between 300°C and 500°C, but did not explore possible modifications of the disordered structure and electrochemical properties before decomposition either.[19] In turn, Blumenhofer et al. and Moghadam et al. reported improvements in the cycle life of $Li_2Ti_{1/3}Mn_{2/3}O_2F$ and $Li_2Mn_{0.5}V_{0.5}O_2F$ with annealing under reducing conditions and posited that they were due to increased structural symmetry and reduced defect concentrations, but without specific structural details.[21,22] Given the paucity of studies in such a wide compositional space, a comprehensive understanding of the thermal evolution of highly fluorinated DRS materials remains elusive, especially in relating phase stability, local arrangements and electrochemical performance.[22]

In the present study, we probed the stability and structural evolution of three highly fluorinated DRS oxyfluorides, Li_2MnO_2F[23], Li_2CoO_2F and Li_2NiO_2F[24], after heating in Ar, an inert atmosphere. We also evaluated the impact of heat-treatment on structural arrangements using a combination of diffraction and spectroscopy,[25,26] and their influence on the electrochemical response. All materials decomposed into ternary oxides and LiF below 500°C, with the exact temperature correlating with how prone to reduction the metal is even under inert atmosphere due to the low partial pressure of O_2. Heat treatment also induced changes in local structure, particularly the cation environments. In the case of Li_2CoO_2F, we found evidence that the initial metastable state involves a highly unusual mixed spin state of Co^{3+}. Furthermore, we observed that the electrochemical response of the materials was notably sensitive to the observed changes in the local environment. The results indicate that these materials are challenged by their stability, but that there is a wealth of intricate local patterns of coordination that could be harnessed to further tune the properties of this novel class of materials.

2. Results and Discussion:

Stability of Li_2MO_2F with temperature. The DRS oxyfluorides Li_2CoO_2F, Li_2MnO_2F, and Li_2NiO_2F were synthesized using a ballmilling method (see methods). The X-ray diffraction (XRD) patterns of three targeted DRS oxyfluorides (**Figure 1** and **S1**) can be indexed to a disordered rock salt phase with Fm-3m space group.[23,24] No crystalline impurities were observed

in the as-synthesized materials. We note that this report constitute the first observation of Li_2CoO_2F in the literature, to the best of our knowledge.

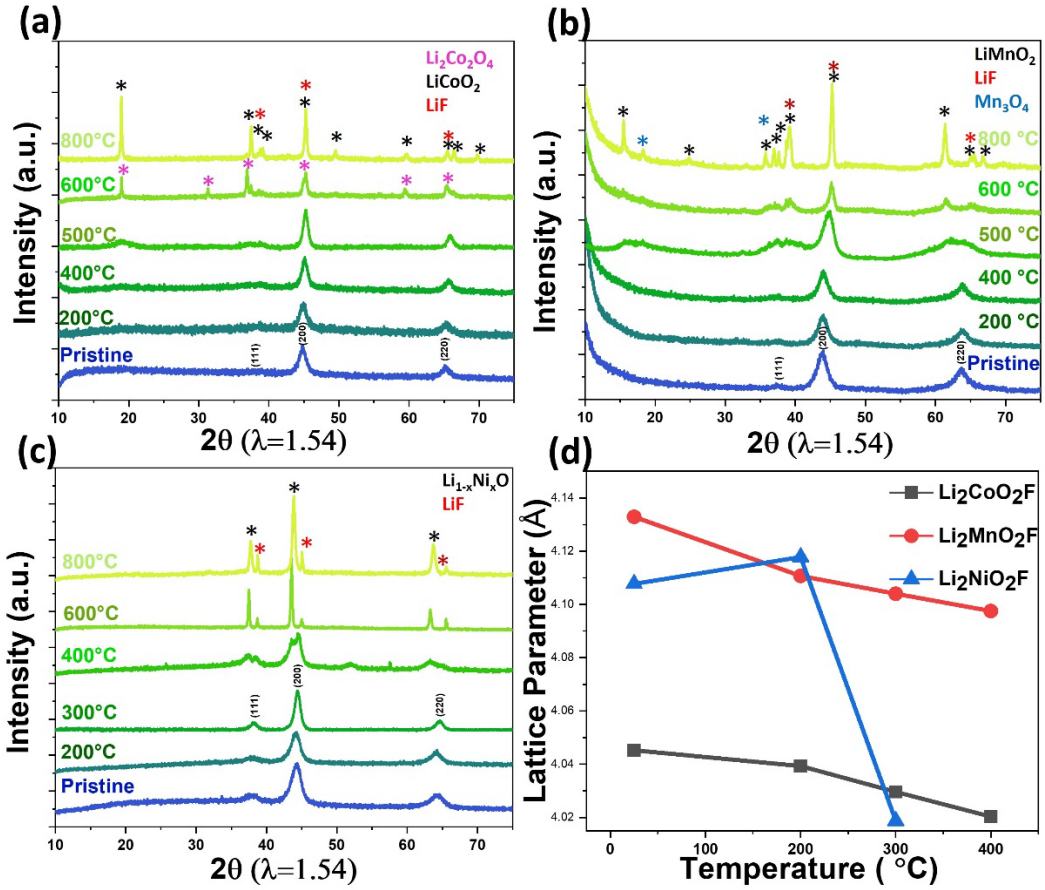

Figure 1. Ex-situ XRD patterns of as-synthesized (pristine) and annealed (up to 800°C) a) Li_2CoO_2F, b) Li_2MnO_2F, c) Li_2NiO_2F, and d) change in lattice parameters upon heating before the onset of decomposition. The Li_2MO_2F samples were annealed under Ar, with a heating rate of 5°C/min, followed by a hold of 1 minute at the target temperature.

Figure 1a shows the ex-situ powder XRD patterns of pristine and heat-treated Li_2CoO_2F. At 200, 400, and 500°C, the patterns could all be fitted with a Fm-3m lattice (**Figure S2**), consistent with a DRS phase, albeit with visible broad features at 19 and 36°, 2θ, at 500°C. After annealing at 600°C, the patterns were best matched to spinel $Li_2Co_2O_4$ and rocksalt LiF, suggesting phase separation occured between 500 and 600°C. After annealing at 800°C, the ternary oxide transformed to layered $LiCoO_2$, still concurrent with LiF. The XRD patterns of pristine and annealed Li_2MnO_2F are shown in Figure 1b. After annealing up to 400°C, a DRS phase was observed (Figure S2), with an onset of phase separation at higher temperature clearly visible when

reaching 500°C, as indicated by new signals at ~18° and 38° 2θ. The phase separation was incomplete even up to 600°C. Li_2MnO_2F decomposed completely into the orthorhombic layered polymorph of $LiMnO_2$, LiF, and a small amount of Mn_3O_4 at 800°C. In the case of the Li_2NiO_2F (Figure 1c), the DRS phase was observed after annealing up to 300°C, but splitting of the rocksalt reflections took place at 400°C, showing the onset of phase separation. The phase separation was partial at 600°C, and a completely decomposed product was seen at 800°C with $Li_{1-x}Ni_xO$, which is also a disordered rocksalt below x~0.39,[27] and LiF (Figure 1c). These results indicate that Li_2CoO_2F and Li_2MnO_2F are stable thermally up to 400°C, compared to up to 300°C for Li_2NiO_2F. The overall decomposition reactions from pristine to fully decomposed products are summarized as follows:

$$Li_2CoO_2F \rightarrow LiF + {}^1/_2\, Li_2Co_2O_4 \quad (1)$$

$$Li_2MnO_2F \rightarrow LiF + o - LiMnO_2 \quad (2)$$

$$Li_2NiO_2F \rightarrow LiF + Li_{1-x}Ni_xO + {}^1/_2\, O_2 \quad (3)$$

Changes in the DRS oxyfluorides prior to phase separation. It is instructive to note that the decomposition of Li_2NiO_2F involves the reduction of the material, likely driven by the higher stability of Ni^{2+} than Ni^{3+} in Ar, whereas Mn^{3+} and Co^{3+} should remain largely stable. This hypothesis was confirmed by Mn, Ni, and Co K-edge X-ray absorption spectroscopy (XAS). Comparisons were made of the samples prior to and after decomposition to the ternary oxides and LiF (**Figure 2**). The spectra are dominated by the leading absorption edge involving an electronic transition from an occupied 1s level to empty valence 4p bands, higher states and the continuum.[28] The energy position of the leading edge, to a first order, reflects changes in formal oxidation state of the metal. Comparison of spectra from Li_2CoO_2F and Li_2MnO_2F that have a preserved DRS framework with spectra from $LiCoO_2$ and o-$LiMnO_2$ (following decomposition after annealing at 800°C) reveal no visible shift in the edge position (Figures 2a and 2b), confirming that both Co and Mn were in their +3 oxidation state throughout the annealing/decomposition process. In contrast, the Ni K-edge XAS (Figure 2c) shows a shift towards lower energy after annealing at 400°C and 600°C, indicating the reduction of Ni, consistent with the reaction proposed in (3).

It is interesting to note that the cell parameters of the as-made compounds, extracted from fits of the XRD data (Table S2 and Figure S2), did not follow a sequence implied by the contraction of the ionic radii from Mn^{3+} to Co^{3+} to Ni^{3+},[29] since Li_2CoO_2F (4.04Å) displayed a smaller value than both Li_2MnO_2F (4.15Å) and Li_2NiO_2F (4.10Å). This observation suggests that despite having the same long-range structure, there are differences in the local arrangement of the ions in these three compounds. There was a linear decrease in the lattice parameters of Li_2CoO_2F and Li_2MnO_2F after annealing up to 400°C, by 0.85 and 0.34%, respectively, consistent with their shift to a higher 2Θ value. The observation that the DRS structure is preserved and that Co/Mn maintains a Co^{3+}/Mn^{3+} state at these temperatures further suggest subtle structural rearrangements in the oxyfluoride with temperature for these two cases. However, in the case of Li_2NiO_2F, all the peaks

moved to a lower 2θ value, corresponding to a slight expansion of the unit cell by 0.24 % after it was annealed to 200°C. Further annealing to 300°C induced a contraction of 0.6% (Table S1).[28,30] The evolution of the cell parameter indicates a more complex rearrangement with temperature in this phase, perhaps due to the reduction of Ni, compensated by formation of O vacancies, even at low temperature.

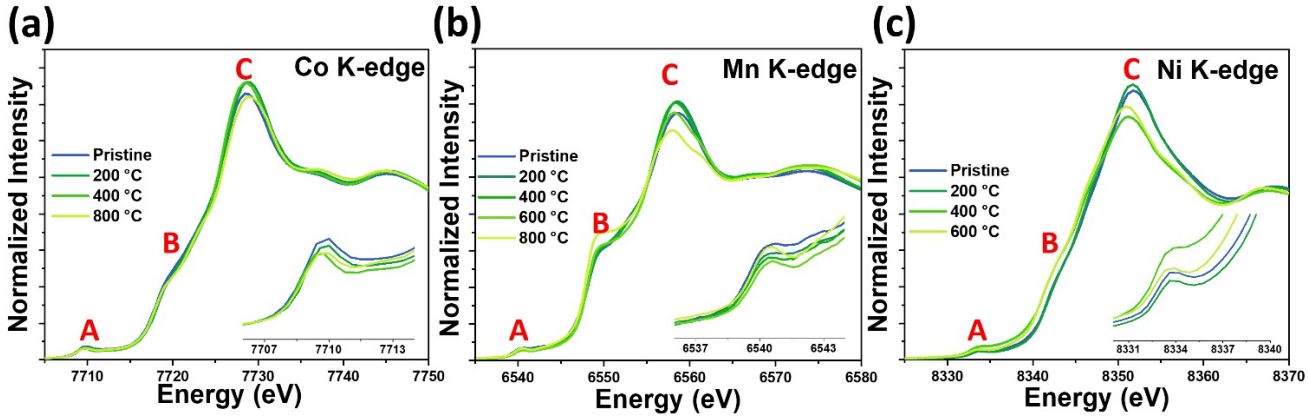

Figure 2. Normalized a) Co K-edge, b) Mn K-edge and c) Ni K-edge XAS of the respective Li_2MO_2F after annealing at the indicated temperatures.

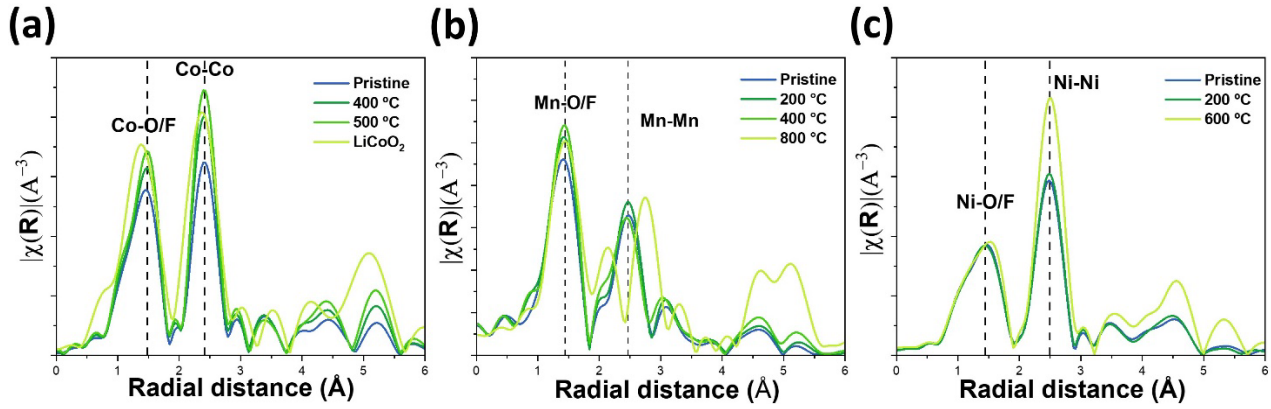

Figure 3. a) Co, b) Ni, and c) Mn K-edge Fourier transform magnitude of k^2-weighted EXAFS spectra of Li_2CoO_2F, Li_2NiO_2F, and Li_2MnO_2F, respectively, after heat treatment at the indicated temperatures.

Effects of annealing on the local structure of transition metals. Closer analysis of the transition metal K-edge XAS provided further indication of the subtle changes indicated by the XRD in the local structure of the DRS oxyfluorides. All materials showed a monotonic decrease in intensity of the weak pre-edge (feature A) upon annealing up to their decomposition temperature, followed by increases after phase separation that were most pronounced in the case of Mn. This can be

interpreted in the context of the nature of the pre-edge feature in K-edge XAS from transition metal compounds, which is a combination of weak quadrupole 1s→3d transitions and dipole-allowed 1s→p transitions into a small fraction of p-character that is mixed into the 3d states of the transition metal. In an ideal octahedral environment, the mixing of p-states with d-states is not allowed, resulting in a pre-edge that is solely from the very weak quadrupole transitions. But in the presence of non-centrosymmetric distortions in the local coordination, 3d and p orbitals are allowed to mix, which will open up the dipole allowed transition into the p-like character of the hybridized 3d states. This makes the overall pre-edge intensity (relative to the main peak) sensitive to centrosymmetric distortions.[31–33] Thus the decrease in pre-edge intensity hints that the octahedral environment of the three metals undergoes subtle geometric changes upon annealing before decomposition occur.

After the onset of the main absorption event, shoulders (feature B) were always observed before the whiteline peak (feature C). No changes were observed for Li_2NiO_2F prior to the reduction of Ni. In contrast, subtracting the Co K-and Mn K-edge XAS of pristine from all the spectra of annealed materials revealed differences in these two features (Figure S3a and b), with different trends upon annealing up to 400°C compared to 800°C. The subtle changes further indicate that the Co environment in the DRS Li_2CoO_2F changes upon annealing, even before decomposition, yet in a way that is distinct from the $LiCoO_2$ end product. The B and C features showed a pronounced variation in the case Li_2MnO_2F. Up to 400°C, there was a slight increase in the intensity of the B feature and a slight decrease in the peak intensity of the C feature. After decomposition, the B feature looked more pronounced, and the white line peak intensity was lower than all other Li_2MnO_2F. This indicates the formation of Mn^{3+} in a different local environment in o-$LiMnO_2$ compared to pristine or annealed Li_2MnO_2F. Figure S4 shows comparison of normalized metal K-edge XAS of the respective Li_2MO_2F with standards.

The extended X-ray absorption fine structure (EXAFS) can be used to obtain the local arrangements around the absorbing atom.[34,35] All Fourier-transform magnitude EXAFS showed two prominent peaks under 3 Å (**Figure 3**a-c), associated with the TM-O/F and TM-TM path interactions (TM = Mn, Co, and Ni). Here, O and F cannot be differentiated since both have very similar scattering factors. The first and second coordination shells of Co, Ni, and Mn changed differently upon annealing the respective oxyfluorides. At the Co center, heat treatment caused a significant increase in the peak intensity of Co-O/F and Co-Co coordination shells, which was concurrent with a decrease in the Debye-Waller factor extracted from fits of the data (Figure S5 and Table S2-4). These observations are consistent with a less disordered, more symmetric Co environment upon annealing as indicated by the K-edge XAS pre-edge intensity discussed above. Both pristine and annealed Li_2CoO_2F had slightly longer Co-O/F distances compared to $LiCoO_2$ after decomposition. Likewise, when going from pristine to annealed Li_2MnO_2F (Figure 3b), the amplitude of the first coordination shell increased and its Debye-Waller factor decreased (Table S2-4), suggestive of a less disordered environment around Mn. The amplitude of the second coordination shell remained roughly unchanged. The Mn K-edge EXAFS of o-$LiMnO_2$ in the

sample annealed at 800°C showed greater complexity, with more peaks observed as a result of corrugation of the layered structure.[36] These structural features appeared to be frustrated in all Li_2MnO_2F samples, consistent with the long-range disorder displayed in the XRD pattern. Lastly, in the case of Li_2NiO_2F (Figure 3c), the only difference upon annealing, and versus the decomposed oxide, was an increase in intensity of the second coordination shell with a slight decrease in Debye-Waller factor.

Despite the absence of any major changes in formal oxidation state upon annealing, the indicated small changes in local structure of Co and Mn could be associated with important changes in the local electronic structure. To this end, we employed XAS to probe the direct transition into the valence orbitals, i.e., metal $L_{2,3}$-edge XAS probing the 3*d* states (2*p*→3*d*) and the ligand K-edge XAS probing 2*p* states (1*s*→2*p*). Both techniques are sensitive to the TM 3*d* to ligand 2*p* hybridization, and a powerful probe of the symmetry and valence of transition metal compounds (**Figure 4**).[37,38] The metal L-edge spectra are split into two regions, L_3 and L_2,[39] due to the TM 2*p* spin-orbit coupling. While the intensity is dominated by the unoccupied 3*d* states and the associated energetics, there are strong effects that give rise to multiplet structures resulting from the local crystal fields, the symmetry of the local environment, and the degree of TM 3*d*-O 2*p* hybridization. The O and F K-edge XAS can access the same hybridized TM 3*d*-ligand 2*p* states, reflected as a pre-edge in the K-edge spectrum, below 534 eV and 686 eV for O and F. This pre-edge has a different character than the 2*p*→3*d* transitions in the TM L-edge, in that the effect of the core-hole in the final state is much smaller, thus being a more innocent probe of the ground state electronic structure of the hybridized orbitals. Its shape and intensity reflects the expected distribution of unoccupied states, which can, in many cases, be derived from simple crystal field theory (e.g., we observe directly the T_{2g} and E_g states as two peaks in the case of an octahedral field).[37,40] Above the pre-edge, a signal corresponding to the absorption edge results from the promotion to hybridized states with TM 4sp, followed by photoionization and multiple scattering.

We will focus on spectra collected in total fluorescence yield (TFY) mode, which probes >100 nm into the material and is less confounded by surface impurities than total electron yield (TEY, **Figure S6**). In the case of Li_2NiO_2F, changes in these spectra (Figures 4g-i) were mostly observed after decomposition at 400°C. The decrease in peak intensity at 853.4 eV at the expense of a second feature at 855.1 eV in the Ni $L_{2,3}$-edge (Figure 4g) and the decrease in intensity of the pre-edge peak at 528 eV in the O K-edge indicate a clear reduction of Ni^{3+},[41–43] consistent with the Ni K-edge data. Since the trends are dominated by such aforementioned reduction, they will not be discussed further.

Figure 4a shows the Co $L_{2,3}$-edge XAS of pristine and annealed Li_2CoO_2F. Here we focus on the main L_3 feature and note the presence of a shoulder on each side of the main peak at 781 eV, centered at 779.2 eV and 782.9 eV, respectively. The $3d^6$ configuration of Co^{3+} can be found both in a low-spin (LS, all 6 electrons in the t_{2g} orbital) or in a high-spin (HS) state, depending on the interplay between the crystal field splitting between t_{2g} and e_g orbitals, the hybridization strength, and the Pauli repulsion. Thus, the electronic structure of Co^{3+} shows a high degree of sensitivity

to small changes in bond length and local distortions. Several studies have established the sensitivity of the Co L_3-edge to spin configurations in octahedral environments associated with the presence of the low-energy (for HS configurations) or high-energy shoulder (for LS). They include evaluations of temperature dependence in $LaCoO_3$,[44] pressure dependence in layered perovskite $LaSrCoO_4$,[45] and several chemical substitutions associated with lattice distortions that can create spin instabilities.[46] In our data for the pristine state of Li_2CoO_2F (Figure 4a), significant shoulders were present on both sides of the main edge, indicating the existence of a mixture of high and low-spin Co^{+3}. When annealed to elevated temperatures, the shoulder at 779.2 eV progressively vanished while the high-energy shoulder became more pronounced, which can be ascribed to a transition from HS-Co^{3+} into predominantly LS-Co^{3+}. Moreover, especially for $3d^6$ systems, the electronic redistribution between t_{2g} and e_g in HS to a full occupancy of the t_{2g} for LS is associated with very different O K-edge pre-edge features,[37] as evidenced by literature data for Sr_2CoO_3Cl and $Li_2Co_2O_4$.[46] The O K-edge XAS of pristine Li_2CoO_2F in Figure 4b showed an intense pre-edge feature at 530.3 eV which decreased in intensity after annealing up to 400°C. We associate this with the presence of a significant fraction of HS-Co^{3+} in the pristine state, which progressively turn into a low-spin state as a function of annealing, consistent with a more well defined local octahedral structure associated with a larger crystal field splitting between t_{2g} and e_g. We also note that the $L_{2,3}$-edge of the pristine Li_2CoO_2F had a very minor feature at 777.5 eV that is not present at higher temperature. Its origin is unclear, but it could possibly be attributed to the presence of a very small amount of Co^{2+} species before annealing.

In the case of high-spin Mn^{+3}, a d^4 ion, the spin-up t_{2g} states are all occupied with one electron, with only one in one e_g state, creating a Jahn-Teller (JT) ground state that induces a tetragonal distortion of the octahedral field.[47] The Mn $L_{2,3}$-edge XAS of all Li_2MnO_2F (Figure 4d) spectra showed an absorption feature centered around 642 eV, with an overall shape that bore close resemblance to octahedral Mn^{3+} reference compounds such as $LaMnO_3$.[48–50] The Mn $L_{2,3}$-edge after decomposition (annealed at 800°C) showed a spectrum with striking resemblance to $LiMnO_2$ which also has a significant tetragonal Jahn−Teller distortion[51] with similar splitting energy of the e_g states,[52–54] even though its long-range structure is clearly different. Although the overall weight of the spectrum remains similar for all spectra, indicating that the electronic structure is not significantly modified, fine spectral features at 640.8, 642.1, and 642.7 eV were altered with temperature, an indication of local electronic structure changes. Comparison of the Mn $L_{2,3}$-edge XAS of Li_2MnO_2F with MnO (**Figure S7**) revealed that the feature at 640.8 eV did not correspond to the most intense signal of Mn^{2+}. Rather, we interpret the changes of the spectral features at 642.1 and 642.7 in relation 640.8, 642.1, and 642.7 eV based on the similar trends reported by Noa et al. when going from octahedral to increasingly tetrahedral Jahn-Teller distortions in spinel oxides containing Mn^{3+}.[52–54] Following the sensitivity of these spectral features, we hypothesize that the Jahn-Teller distortions in Li_2MnO_2F are nearly intact upon annealing with a potential slight loss of order between 200 and 400°C.

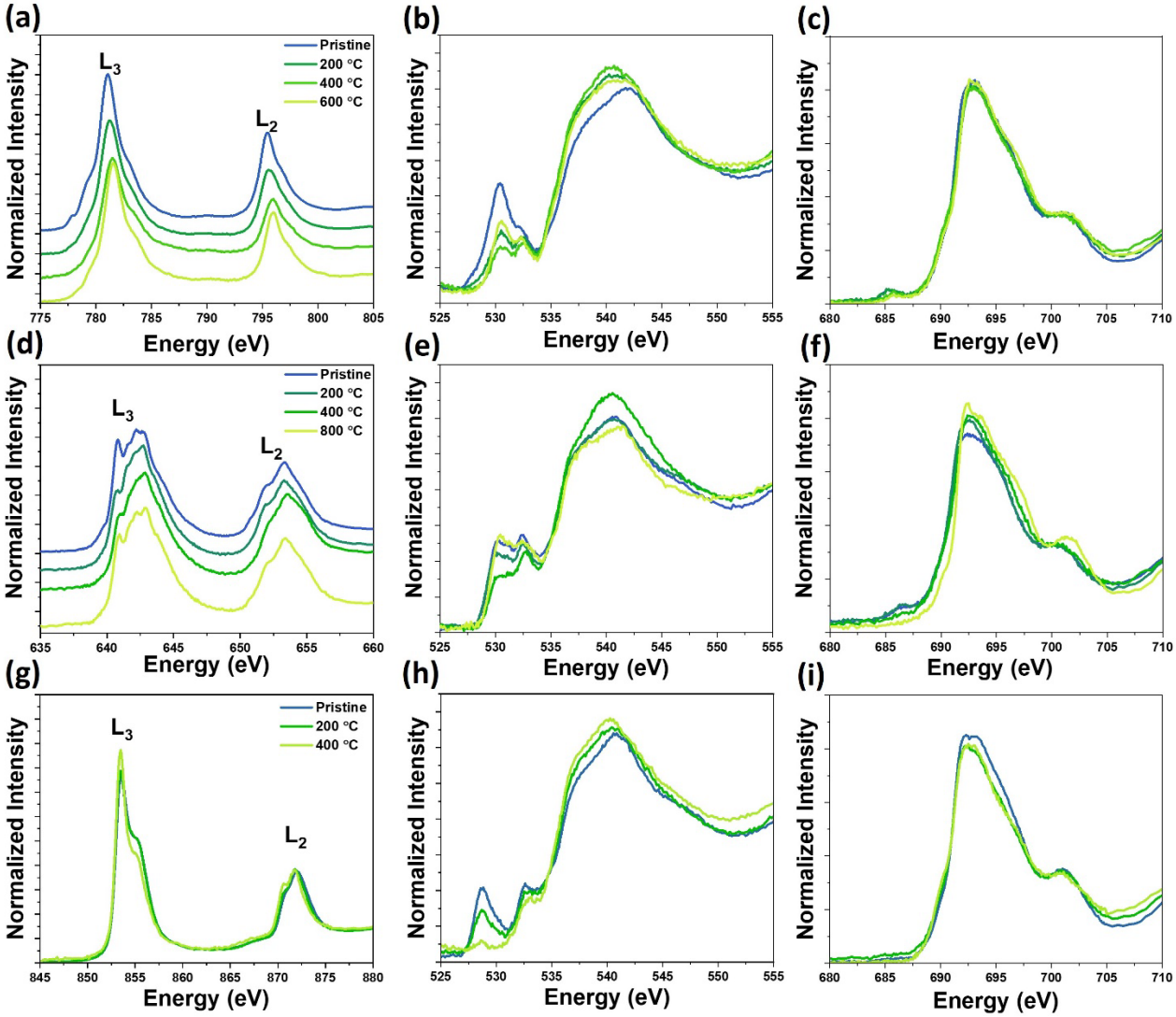

Figure 4. a-c) Co L-edge, O K-edge, and F K-edge XAS of pristine and annealed Li_2CoO_2F; (d-f) Mn L-edge, O K-edge and F K-edge XAS pristine and annealed Li_2MnO_2F; and (g-i) Ni L-edge, O K-edge and F K-edge XAS pristine and annealed Li_2NiO_2F as a function of annealing temperature. All the spectra were collected in TFY mode. (XAS in TEY mode for all samples are plotted in Figure S5).

The O K-edge XAS of Li_2MnO_2F (Figure 4e) shows two pre-edge features, one asymmetric at 530.2 and a symmetric and sharper one at 532.4 eV. Much like the Mn $L_{2,3}$-edge XAS, the O K-edge XAS of o-$LiMnO_2$ in the decomposed sample was very similar to pristine Li_2MnO_2F and a tetragonally distorted Mn^{3+} reported by Noa et al.[52] The annealed spectra show very similar features, but we note that the 400°C show a slight loss of pre-edge intensity which could indicate a loss of tetragonal distortion due to a slight loss of order, in accordance with the Mn $L_{2,3}$-edge results.

Atomic rearrangements within the DRS framework induced by annealing. The existence of signals between 685 and 687 eV in the F K-edge XAS of pristine Li_2CoO_2F and Li_2MnO_2F (Figure 4c and f) confirms the existence of Co/Mn 3d-F 2p covalent bonding.[40] The lower intensity of all pre-edge signals compared to the O counterparts was ascribed to a weaker overlap of metal-anion states, and it hampered any analysis of their fine structure. However, a decrease in pre-edge intensity and a sharpening of the edge signals at 692 eV was observed upon annealing in all materials (Figures 4c, f and i), which suggested a reorganization of the structure toward less prevalent M-F bonds, implying that temperature favored the formation of more Li-F and M-O bonds until phase separation into the ternary oxide and LiF. Indeed, the F K-edge shape of Li_2CoO_2F and Li_2MnO_2F at 800°C shows no pre-edge feature and a change in edge shape that made it very reminiscent of pure LiF,[55–57] consistent with the XRD data. Li_2NiO_2F had much weaker intensity in the pre-edge region (Figure 4i) but displayed a higher background below 690 eV compared to the spectrum of LiF (Figure S8).

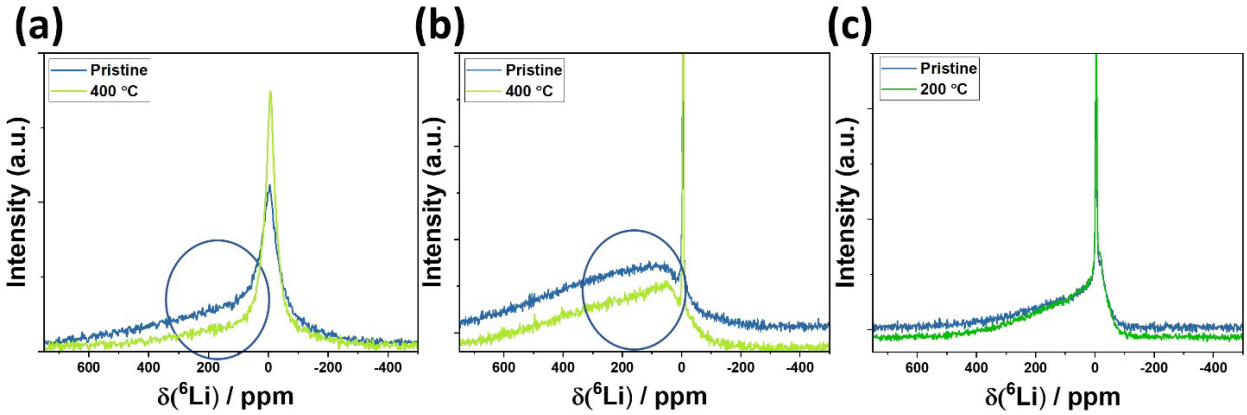

Figure 5. ^{6}Li NMR spectra obtained on pristine and annealed (a) Li_2CoO_2F, (b) Li_2MnO_2F and (c) Li_2NiO_2F. The temperatures of annealing are indicated in the legend.

^{6}Li solid state NMR spectroscopy provided further insight into the changes in the local DRS structure from the perspective of Li environments because it is particularly sensitive to them in the presence of paramagnetic transition metals, with the spectra generally varying over large shift windows in the presence of hyperfine (or Fermi-contact) interactions.[58–60] This aspect unlocks detailed information on the oxidation state of the transition metal and its distribution (number and geometric arrangements) around Li. **Figure S10** displayed full ^{6}Li NMR spectra for Li_2CoO_2F, Li_2MnO_2F and Li_2NiO_2F. As shown in **Figure S9**, the ^{6}Li NMR data for pristine and annealed Li_2CoO_2F samples displayed a major peak at ~0 ppm with a large, broad shoulder around 200 ppm and a small shoulder around -50 ppm. A typical ^{6}Li NMR spectrum of stoichiometric $LiCoO_2$ only shows a resonance at around 0 ppm due to lithium in a diamagnetic local environment in the presence of LS (t_{2g}^6) Co^{+3} ions.[61] It is worth noting that signals in this region can also arise from unreacted lithium salts or LiF domains. The additional peaks well outside this region further support that lithium is surrounded by Co^{+3} in a mixture of HS and LS configurations, consistent

with the observations from XAS above, because HS would lead to unpaired electrons that induce hyperfine interactions. The fact that the observed peaks are broad indicates the presence of different lithium local environments due to structural disorder. Annealing introduced two main changes: reduction in peak broadening and intensity of the hyperfine peaks (200 and -50 ppm) and increase in the intensity at 0 ppm. These changes are due to an increase in order and the enrichment in LS Co^{+3} in the structure as the annealing temperature was increased, possibly accompanied by rearrangement of Co and Li to start forming larger local $[LiF_6]_n$ and $[CoO_6]_n$ clusters as precursor to phase separation into $Li_2Co_2O_4$ and LiF at higher temperature. It is worth noting that hyperfine signals associated with HS Co^{3+} were visible even after annealing at 400°C (**Figure 5a**), suggesting that NMR is more sensitive to them than Co $L_{2,3}$-edge XAS because they are easier to resolve from LS configurations. **Figure S11** displayed deconvolution of the ^{6}Li NMR spectrum of Li_2CoO_2F (a) in its pristine state and (b) after annealing at 400°C

As shown in Figure 5b, the spectra for all phase-pure Li_2MnO_2F were dominated by a broad peak ranging from 0 ppm to 600 ppm for Li environments with varying Mn coordination in the bulk of the material. The deconvolution (**Figure S12**) of this broad peak suggested that there are at least three main resonances at ~ 60, 240 and 480 ppm), which, based on the literature, we assigned to the presence of 1 to 3 Mn^{+3} within the first and second shells of cations around Li.[58] The sharp peak at 0 ppm is due to diamagnetic Li, convoluting signals from Li-rich domains within the DRS and impurities. As the annealing temperature was increased to 400°C, the peaks got sharper and well resolved suggesting an increase in overall order within the structure. The center of gravity subtly moved toward lower shifts, indicating that the amount of Mn^{3+} around Li decreased, consistent with an increased local segregation of $[LiF_6]_n$ and $[MnO_6]_n$ clusters prior to phase separation.

The ^{6}Li NMR spectra of Li_2NiO_2F did not discernibly change at temperatures where a single phase could be found in the XRD patterns (Figure 5c). Apart from the sharp peak at 0 ppm for diamagnetic Li environments due to Li-rich domains and any impurities, there was evidence of Li locally surrounded with Ni^{+3} in the form of broad and asymmetric peaks ranging from 0 to 400 ppm and 0 to -50 ppm. The asymmetric peak shape and broad nature of the peaks are due to disorder in the structure and distribution of different Li environments coordinated to Ni^{+3} ions in varying configurations.[24] The deconvolution of the spectra suggests presence of lithium with 1 to 2 Ni^{+3} in both first and second cation shells (Figure S13).

^{19}F solid-state NMR was also measured to track the existence of F species surrounded by Li and, indirectly, transition metals, for all the samples (**Figure S14**). All ^{19}F NMR spectra showed a major peak at ~ -204 ppm for F environments surrounded by Li, accompanied by spinning sidebands. Compared to phase-pure LiF,[25] all oxyfluorides showed broader peaks, and stronger and widely spanning sidebands due to electron-dipolar interaction between F and paramagnetic metal centers in the bulk. Direct TM-F coordination (TM in 1st and 2nd coordination) would likely generate peaks that are too broad and/or shifted to capture experimentally.[26] However, in the case of Li_2MnO_2F, the pristine state displayed a complex and extremely broad background which could not be fully

captured in the conditions of the experiment. A similar broad peak formation was also reported by House et al. and was attributed to F presence in rock salt lithium manganese oxyfluorides.[23] The presence of a broad background challenged accurate analysis of relative intensities in this spectrum. However, annealing led to increases in intensity of the main peak at -204 ppm, consistent with a tendency toward segregation of increasingly large $[LiF_6]_n$ domains prior to full phase separation indicated by F K-edge XAS and ^{6}Li NMR. Annealing Li_2MnO_2F also greatly alleviated the large background in the spectra, which would further add to the evidence of increasing clustering of Li-rich and Mn-rich domains prior to long-range phase separation.

Evolution of electrochemical metrics of the DRS phases upon annealing. Voltage-composition profiles were measured galvanostatically at a C/20 rate in Li metal half-cells. **Figure 6** shows the first cycles of the pristine and annealed DRS oxyfluorides whereas up to 5 cycles are displayed in **Figures S15** to **S17**. Starting upon oxidation, the cell with Li_2CoO_2F showed a sloping feature with an average voltage of ~3.85 V vs. Li^+/Li^0, accumulating capacity equivalent to removing ~1.1 Li per mol of the compound, assuming 100% faradaic efficiency (Figure 6a). The corresponding dQ/dV curves (Figure 6d) showed two broad processes centered at 3.8 V and at 4.2 V, followed by a tail at the highest potential. Upon reduction, the slope of the potential-composition profile notably increased, followed by bending to an even steeper slope below 2.9 V. There was only one broad peak at 3.4 V in the dQ/dV plot. At 1.5 V, the total capacity was equivalent to 1.0 mol of Li per mol of the compound, indicating a coulombic efficiency higher than 90%. Upon further cycling, the broad peak at 4.2 V during oxidation in dQ/dV plot disappeared, indicating its irreversibility, which led to rather symmetric profiles upon cycling (Figure S14 d). The annealed samples showed similar levels of activity and the electrochemical profile of Li_2CoO_2F at 200°C displayed similar features to the pristine. However, there was a noticeable decrease in voltage hysteresis for Li_2CoO_2F annealed at 400°C. This decrease was clear in the dQ/dV plot, which revealed that the reduction peak approached the voltage of the oxidation process, likely due to improved electrochemical kinetics, and the disappearance of the irreversible high voltage peak during oxidation from pristine to 400°C (Figure 6d).

The capacity of pristine Li_2MnO_2F upon oxidation to 4.8 V vs. Li^+/Li^0 was equivalent to removing ~1.3 mol of Li per mol of compound (Figure 6b), associated with a broad process at 3.5 V vs. Li^+/Li^0 in the dQ/dV plot (Figure 6f). A similarly broad process at 3.3 V was found on the subsequent reduction, followed by bending of the profile below 2.7 V to almost completely reverse the charge capacity. The voltage profiles of the pristine material and upon annealing at 200°C shared features. In contrast, the material annealed at 400°C delivered ~1.1 mol of Li of the compound upon oxidation and a greater portion of its reversible capacity above 2.7 V than the pristine state, indicating a decrease in voltage hysteresis. The corresponding derivative plots in Figure 6e show a sharpening of the main peaks associated with oxidation and reduction. We interpret this narrowing of the spread of voltages of the reaction as resulting from an increased structural ordering in the compound, leading to Li sites with equivalent chemical potentials. Concurrently, both oxidation and reduction peaks visibly shifted towards lower voltage, reflecting

a decrease in the equilibrium voltage of the compound. We hypothesize that this decrease is associated with the changes in the magnitude of the Jahn-Teller distortion of Mn^{3+} revealed by Mn $L_{2,3}$-edge XAS. While the consequence of slightly lower voltages is a slightly lower energy density in the compound, this change is accompanied by a decrease in hysteresis that, in turn, increases energy density. All profiles experienced a slight decrease of the oxidation and reduction potential in cycle 2 followed by stable electrochemical profiles thereafter (Figure S16).

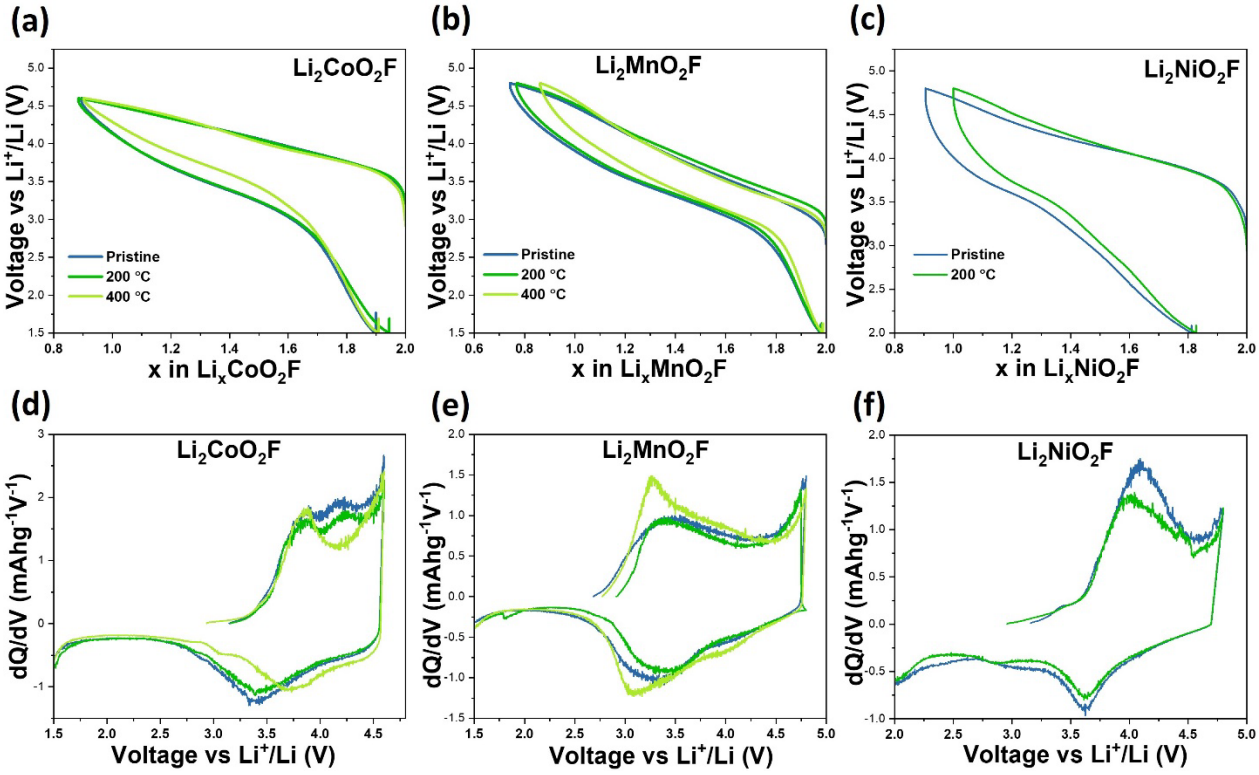

Figure 6. Voltage vs. composition (a-c) and corresponding dQ/dV vs. voltage (d-f) traces of Li metal half-cells with Li_2CoO_2F, Li_2MnO_2F, and Li_2NiO_2F as working electrodes, respectively. The temperatures of annealing are indicated in the legends. The change in x in (a-c) assumes 100% faradaic efficiency.

Upon oxidation, pristine Li_2NiO_2F displayed an average voltage of 3.85 – 3.9 V vs. Li^+/Li^0, with an associated capacity of ~1.1 mol of Li of the compound (Figures 6c and f). During reduction, the change to a steeper slope took place below 3.4 V with ~0.2 mol Li being irreversible. Compared to the Co and Mn counterparts, Li_2NiO_2F delivered a much smaller fraction of its discharge capacity before the profile bent to a higher slope and greatly deviated from the profile on oxidation, for the highest hysteresis of all materials tested. Annealing Li_2NiO_2F at 200°C only decreased the total accumulated capacity on oxidation, leading to a higher coulombic efficiency, with no

observable change in the overall profile. This behavior agrees well with this material experiencing the smallest change in overall local structure upon annealing. All Li_2NiO_2F samples experienced a decrease in the voltage of oxidation in the second cycle, with profiles being stable thereafter (Figure S17).

3. Conclusion:

We investigated the stability of the disordered rock salt arrangement of Li_2CoO_2F, Li_2MnO_2F, and Li_2NiO_2F by annealing under an inert atmosphere and combining diffraction, spectroscopy and electrochemical tests. Whereas Li_2CoO_2F and Li_2MnO_2F remained as single phases up to 400°C, Li_2NiO_2F decomposed into a ternary oxide and LiF above 300°C. Metal K-edge XAS measurements indicate that Li_2CoO_2F and Li_2MnO_2F maintain a stable oxidation state throughout, with the lower stability of Li_2NiO_2F seemingly driven by its propensity to reduce as phase separation occurs. A comprehensive analysis of XAS and NMR data revealed the existence of an unusual high spin state of Co^{3+} in pristine Li_2CoO_2F which is removed upon annealing. In turn, temperature induced a changes in the Jahn-Teller distortion of Mn^{3+} within the disordered rocksalt. These modifications of the $[MX_6]$ (M=Mn, Co, Ni; X=O, F) octahedral symmetry are accompanied by a decrease in the extent of structural disorder in the rocksalt upon annealing, with the formation of local clusters of $[LiF_6]_n$ and $[MO_6]_n$ that precede the phase separation into the ternary oxide and LiF. The subtle atomic rearrangements influenced the electrochemical response of the DRS oxyfluorides. There was an overall decrease in voltage hysteresis and a small, yet visible improvement in energy efficiency. In the case of Li_2MnO_2F, annealing also decreased the equilibrium voltage and narrowed the voltage spread of the cycling process. All in all, our results suggesting that structural rearrangements via careful annealing treatments offer a way to further tune local atomic arrangements of Li-rich DRS oxyfluoride materials and, with them, the electrode properties, creating new avenues to fulfill their potential as high-energy-density cathodes for future LIBs.

4. Experimental section:

Material synthesis: Li_2MnO_2F, Li_2CoO_2F, and Li_2NiO_2F were synthesized using high energy mechanochemical ball-milling. Li_2O (Alfa Aesar, ACS, 99% min) and LiF (Alfa Aesar, 99.99%) were mixed with Mn_2O_3 (Alfa Aesar, 99%), $LiCoO_2$ (Sigma-Aldrich, 99.8%) or $LiNiO_2$ in stoichiometric ratios under Ar atmosphere and placed in 50 ml stainless steel jars containing ten balls of 5 mm and five balls of 10 mm. Retsch PM200 planetary ball mill, was used for grinding respective precursors at 500 rpm for 50 hrs. The total amount of the precursor was 1 gm in each jar. $LiNiO_2$ was synthesized by ball milling $Ni(OH)_2$ and LiOH for 3hrs. at 300 rpm followed by

annealing at 750°C for 12 hrs. under oxygen flow. [62] The as-synthesized compounds were annealed at various temperatures in a tube furnace under an Ar atmosphere. The heating rate was 5°C/min with a hold of 1 minute at the targeted temperature.

Powder X-ray diffraction: Synchrotron powder X-ray diffraction patterns were measured for all pristine samples at the 11-BM beamline of Advanced Photon Source (Argonne National Laboratory) with λ = 0.45789 Å. X-ray powder diffraction of all the thermally treated samples were performed using a laboratory Bruker D8 Advance diffractometer operating at 40 kV and 40 mA with Cu K_α radiation (λ = 1.5418 Å). XRD profiling was collected by scanning from 10° to 75°, 2θ, using a step size of 0.019°, at a rate of 2.6 x 10^{-5} °/min 2θ, in a custom air-free sample holder to avoid contamination from the air. Pawley refinement of the XRD patterns was performed using JANA2006.[63]

X-ray Absorption Spectroscopy (XAS): Co, Mn and Ni K-edge XAS was performed at 5 BM-D at the Advanced Photon Source, Argonne National Laboratory. XAS spectra were collected in both transmission and fluorescence modes using ion chambers (FMB-Oxford) and a 4-element Si-drift vortex detector (Vortex-ME4, Hitachi Corp), respectively. The ion chambers upstream and downstream of the sample were filled with 600 He/100 N_2 (Torr) and 1150 He/250 N_2 (Torr), respectively. The third ion chamber that measures the reference foil was filled with 760 Ar (Torr). The incident beam energy was selected by a Si (111) double-crystal monochromator. The beam intensity was detuned to 60 % of its maximum for harmonic rejection. A metal reference foil was measured simultaneously to each sample for energy calibration.A metal reference foil was measured simultaneous to each sample for energy calibration. Data analysis was completed using the IFEFFIT package.[35,64] XAS measurements at the M $L_{2,3}$-, O K- and F K-edges were conducted at the Stanford Synchrotron Radiation Light source (SSRL) bending magnet beamline 8−2 at a 55° incidence angle (magic angle) of X-ray incidence. Beamline 8−2 is equipped with a spherical grating monochromator, operated using 40 × 40 μm2 slits, resulting in a resolution of around 200 meV. The spot size at the interaction point was about 1 × 1 mm^2, and the total flux was 10^{10} photons/s, for which beam damage was not noticeable even for extended exposure. The data were collected both in the total fluorescence yield (TFY), and total electron yield (TEY) modes using the drain current (amplified by a Keithley picoampmeter) and a cylindrical mirror analyzer (CMA) operated with a pass energy of 200 eV and set to record the main Auger line for the various edges, respectively.

NMR: ^{6}Li and ^{19}F MAS NMR experiments were performed at 7.02 Tesla (300 MHz) on a Bruker Avance III HD spectrometer using a 1.3 mm MAS probe, operating at a Larmor frequency of 44.21 MHz and 282.347MHz, respectively. All spectra were acquired at 50 kHz with a rotor synchronized echo pulse sequence (90°-τ-180°-τ-acq), where $\tau = 1/\nu_r$ under a constant temperature of 283 ± 0.1 K. A π/2 pulse width of 1.5 μs was used with sufficiently long pulse recycle delays of 0.2 s for ^{6}Li MAS NMR experiments and chemical shifts were referenced to 1M LiCl at 0 ppm.

A π/2 pulse width of 1.5 μs was used for 19 F NMR experiments with pulse delays of 2s. ^{19}F chemical shifts are given relative to CCl_3F, referenced using a secondary reference of LiF at -204ppm.

Electrochemical measurements: Li metal half-cells were built with the DRS oxyfluorides as active materials in the working electrode. The powders were hand ground (to preserve the morphology) with conductive carbon (Super C65 from Imerys, typical Fe content of 2 ppm) in an 80:20 ratio without binder and used as such in the cells. Each cell had around ~10mg of active material. Li metal foil was used as the counter and pseudo-reference, with two Whatman GF/D borosilicate glass fiber sheets as separator, soaked in an electrolyte composed of 1 M $LiPF_6$ in ethylene carbonate: ethyl methyl carbonate in 3:7 weight ratios. Coin cells were assembled in an Ar glovebox (O_2 < 0.1 ppm, H_2O < 0.1 ppm). Galvanostatic charge–discharge cycling was performed using a BT-Lab tester (Bio-Logic) at room temperature, at a rate of C/20 (indicating an extraction of 1 Li per formula unit in 20 hours). Samples for ex-situ analysis were harvested by stopping the cells at the desired cutoff voltages.

Supporting Information

Supporting Information is available from the Wiley Online Library or from the author.

Acknowledgements

This work was supported by the National Science Foundation (grant no. DMR-2118020). Use of the Stanford Synchrotron Radiation Light source, SLAC National Accelerator Laboratory, was supported by the U.S. Department of Energy, Office of Science, Office of Basic Energy Sciences under Contract No. DE-AC02-76SF00515. XAS measurements were done at 5-BM-D of DND-CAT, which is supported through E. I. du Pont de Nemours & Co., Northwestern University, and Dow Chemical Company. This research used resources of Advanced Photon Source of Argonne National Laboratory is supported by DOE under Contract No. DE-AC02–06CH11357.

Conflict of Interest

The authors declare no conflict of interest.

References

[1] M. S. Whittingham, *Chem. Rev.* **2004**, *104*, 4271.
[2] A. Manthiram, *Nat Commun* **2020**, *11*, 1550.
[3] J. Cabana, L. Monconduit, D. Larcher, M. R. Palacín, *Advanced Materials* **2010**, *22*, E170.
[4] V. Etacheri, R. Marom, R. Elazari, G. Salitra, D. Aurbach, *Energy & Environmental Science* **2011**, *4*, 3243.

[5] E. Fan, L. Li, Z. Wang, J. Lin, Y. Huang, Y. Yao, R. Chen, F. Wu, *Chem. Rev.* **2020**, *120*, 7020.
[6] D. A. Kitchaev, Z. Lun, W. D. Richards, H. Ji, R. J. Clément, M. Balasubramanian, D.-H. Kwon, K. Dai, J. K. Papp, T. Lei, B. D. McCloskey, W. Yang, J. Lee, G. Ceder, *Energy Environ. Sci.* **2018**, *11*, 2159.
[7] Y. Pei, Q. Chen, Y. Ha, D. Su, H. Zhou, S. Li, Z. Yao, L. Ma, K. J. Sanders, C. Sheng, G. R. Goward, L. Gu, A. Yu, W. Yang, Z. Chen, *Angewandte Chemie International Edition* **2022**, *61*, e202212471.
[8] B. Ouyang, N. Artrith, Z. Lun, Z. Jadidi, D. A. Kitchaev, H. Ji, A. Urban, G. Ceder, *Adv. Energy Mater.* **2020**, *10*, 1903240.
[9] Z. Lun, B. Ouyang, D. A. Kitchaev, R. J. Clément, J. K. Papp, M. Balasubramanian, Y. Tian, T. Lei, T. Shi, B. D. McCloskey, J. Lee, G. Ceder, *Advanced Energy Materials* **2019**, *9*, 1802959.
[10] D. Chen, J. Ahn, G. Chen, *ACS Energy Lett.* **2021**, *6*, 1358.
[11] R. J. Clément, Z. Lun, G. Ceder, *Energy Environ. Sci.* **2020**, *13*, 345.
[12] Z. Jadidi, T. Chen, P. Xiao, A. Urban, G. Ceder, *J. Mater. Chem. A* **2020**, *8*, 19965.
[13] M. Mishra, G. S. Taiwo, K. P. C. Yao, *ACS Appl. Mater. Interfaces* **2023**, *15*, 14261.
[14] L. Li, Z. Lun, D. Chen, Y. Yue, W. Tong, G. Chen, G. Ceder, C. Wang, *Advanced Functional Materials* **2021**, *31*, 2101888.
[15] J. Lee, J. K. Papp, R. J. Clément, S. Sallis, D.-H. Kwon, T. Shi, W. Yang, B. D. McCloskey, G. Ceder, *Nat Commun* **2017**, *8*, 981.
[16] J. H. Song, A. Kapylou, H. S. Choi, B. Y. Yu, E. Matulevich, S. H. Kang, *Journal of Power Sources* **2016**, *313*, 65.
[17] X. Wang, Y. Huang, D. Ji, F. Omenya, K. Karki, S. Sallis, L. F. J. Piper, K. M. Wiaderek, K. W. Chapman, N. A. Chernova, M. S. Whittingham, *J. Electrochem. Soc.* **2017**, *164*, A1552.
[18] H. Ji, D. A. Kitchaev, Z. Lun, H. Kim, E. Foley, D.-H. Kwon, Y. Tian, M. Balasubramanian, M. Bianchini, Z. Cai, R. J. Clément, J. C. Kim, G. Ceder, *Chem. Mater.* **2019**, *31*, 2431.
[19] A. Kanno, Y. Ugata, I. Ikeuchi, M. Hibino, K. Nakura, Y. Miyaoka, I. Kawamura, D. Shibata, T. Ohta, N. Yabuuchi, *ACS Energy Lett.* **2023**, 2753.
[20] M. K. Aydinol, A. F. Kohan, G. Ceder, K. Cho, J. Joannopoulos, *Phys. Rev. B* **1997**, *56*, 1354.
[21] I. Blumenhofer, Y. Shirazi Moghadam, A. El Kharbachi, Y. Hu, K. Wang, M. Fichtner, *ACS Mater. Au* **2022**.
[22] Y. S. Moghadam, A. E. Kharbachi, G. Melinte, T. Diemant, M. Fichtner, *J. Electrochem. Soc.* **2022**, *169*, 120514.
[23] R. A. House, L. Jin, U. Maitra, K. Tsuruta, J. W. Somerville, D. P. Förstermann, F. Massel, L. Duda, M. R. Roberts, P. G. Bruce, *Energy Environ. Sci.* **2018**, *11*, 926.
[24] X. Xu, L. Pi, J.-J. Marie, G. J. Rees, C. Gong, S. Pu, R. A. House, A. W. Robertson, P. G. Bruce, *J. Electrochem. Soc.* **2021**, *168*, 080521.
[25] R. J. Clément, D. Kitchaev, J. Lee, Gerbrand Ceder, *Chem. Mater.* **2018**, *30*, 6945.
[26] J. Lee, D. A. Kitchaev, D.-H. Kwon, C.-W. Lee, J. K. Papp, Y.-S. Liu, Z. Lun, R. J. Clément, T. Shi, B. D. McCloskey, J. Guo, M. Balasubramanian, G. Ceder, *Nature* **2018**, *556*, 185.
[27] J. B. Goodenough, D. G. Wickham, W. J. Croft, *Journal of Physics and Chemistry of Solids* **1958**, *5*, 107.
[28] E. Lee, S. Muhammad, T. Kim, H. Kim, W. Lee, W.-S. Yoon, *Advanced Science* **2020**, *7*, 1902413.
[29] R. D. Shannon, *Acta Crystallographica Section A* **1976**, *32*, 751.
[30] J. Albertsson, S. C. Abrahams, Å. Kvick, *Acta Crystallographica Section B* **1989**, *45*, 34.
[31] T. Yamamoto, *X-Ray Spectrometry* **2008**, *37*, 572.

[32] F. Farges, *Phys. Rev. B* **2005**, *71*, 155109.
[33] F. de Groot, G. Vankó, P. Glatzel, *J. Phys.: Condens. Matter* **2009**, *21*, 104207.
[34] A. Jentys, *Phys. Chem. Chem. Phys.* **1999**, *1*, 4059.
[35] B. Ravel, S. D. Kelly, *AIP Conference Proceedings* **2007**, *882*, 150.
[36] J. E. Greedan, N. P. Raju, I. J. Davidson, *Journal of Solid State Chemistry* **1997**, *128*, 209.
[37] F. Frati, M. O. J. Y. Hunault, F. M. F. De Groot, *Chem. Rev.* **2020**, *120*, 4056.
[38] F. M. F. de Groot, M. Grioni, J. C. Fuggle, J. Ghijsen, G. A. Sawatzky, H. Petersen, *Phys. Rev. B* **1989**, *40*, 5715.
[39] C. H. M. van Oversteeg, H. Q. Doan, F. M. F. de Groot, T. Cuk, *Chem. Soc. Rev.* **2017**, *46*, 102.
[40] I. Roy, K. Kumar, H. Li, N. Sunariwal, G. C. B. Alexander, J. W. Freeland, F. Rodolakis, J. Cabana, *Chem. Mater.* **2023**.
[41] J.-S. Kang, S. S. Lee, G. Kim, H. J. Lee, H. K. Song, Y. J. Shin, S. W. Han, C. Hwang, M. C. Jung, H. J. Shin, B. H. Kim, S. K. Kwon, B. I. Min, *Phys. Rev. B* **2007**, *76*, 195122.
[42] C. Tian, D. Nordlund, H. L. Xin, Y. Xu, Y. Liu, D. Sokaras, F. Lin, M. M. Doeff, *J. Electrochem. Soc.* **2018**, *165*, A696.
[43] Z. Yang, L. Mu, D. Hou, M. M. Rahman, Z. Xu, J. Liu, D. Nordlund, C.-J. Sun, X. Xiao, F. Lin, *Advanced Energy Materials* **2021**, *11*, 2002719.
[44] M. W. Haverkort, Z. Hu, J. C. Cezar, T. Burnus, H. Hartmann, M. Reuther, C. Zobel, T. Lorenz, A. Tanaka, N. B. Brookes, H. H. Hsieh, H.-J. Lin, C. T. Chen, L. H. Tjeng, *Phys. Rev. Lett.* **2006**, *97*, 176405.
[45] S. C. Haw, Z. Hu, H. J. Lin, J. M. Lee, H. Ishii, N. Hiraoka, A. Meléndez-Sans, A. C. Komarek, L. H. Tjeng, K. Chen, C. Luo, F. Radu, C. Te Chen, J.-M. Chen, *Journal of Alloys and Compounds* **2021**, *862*, 158050.
[46] J. Zhao, S.-C. Haw, X. Wang, Z. Hu, C.-Y. Kuo, S.-A. Chen, H. Ishii, N. Hiraoka, H.-J. Lin, C.-T. Chen, Z. Li, A. Tanaka, C.-E. Liu, R. Yu, J.-M. Chen, C. Jin, *physica status solidi (b)* **2021**, *258*, 2100117.
[47] I. S. Elfimov, V. I. Anisimov, G. A. Sawatzky, *Phys. Rev. Lett.* **1999**, *82*, 4264.
[48] T. C. Kaspar, P. V. Sushko, S. R. Spurgeon, M. E. Bowden, D. J. Keavney, R. B. Comes, S. Saremi, L. Martin, S. A. Chambers, *Advanced Materials Interfaces* **2019**, *6*, 1801428.
[49] M. Ghiasi, M. U. Delgado-Jaime, A. Malekzadeh, R.-P. Wang, P. S. Miedema, M. Beye, F. M. F. De Groot, *J. Phys. Chem. C* **2016**, *120*, 8167.
[50] Three Oxidation States of Manganese in the Barium Hexaferrite BaFe12–xMnxO19, .
[51] M. G. Herrera-Yáñez, J. A. Guerrero-Cruz, M. Ghiasi, H. Elnaggar, A. de la Torre-Rangel, L. A. Bernal-Guzmán, R. Flores-Moreno, F. M. F. de Groot, M. U. Delgado-Jaime, *Inorg. Chem.* **2023**, *62*, 3738.
[52] H.-J. Noh, S. Yeo, J.-S. Kang, C. L. Zhang, S.-W. Cheong, S.-J. Oh, P. D. Johnson, *Appl. Phys. Lett.* **2006**, *88*, 081911.
[53] L. E. Gontchar, A. E. Nikiforov, S. E. Popov, *AIP Conference Proceedings* **2001**, *554*, 403.
[54] K. I. Kugel', D. I. Khomskiĭ, *Sov. Phys. Usp.* **1982**, *25*, 231.
[55] D. Wang, L. Zuin, *Journal of Power Sources* **2017**, *337*, 100.
[56] J. Vinson, J. J. Rehr, J. J. Kas, E. L. Shirley, *Phys. Rev. B* **2011**, *83*, 115106.
[57] M. Balasubramanian, H. S. Lee, X. Sun, X. Q. Yang, A. R. Moodenbaugh, J. McBreen, D. A. Fischer, Z. Fu, *Electrochem. Solid-State Lett.* **2001**, *5*, A22.
[58] Y. J. Lee, F. Wang, C. P. Grey, *J. Am. Chem. Soc.* **1998**, *120*, 12601.
[59] C. P. Grey, N. Dupré, *Chem. Rev.* **2004**, *104*, 4493.
[60] S. Levasseur, M. Ménétrier, C. Delmas, *J. Electrochem. Soc.* **2002**, *149*, A1533.

[61] S. Levasseur, M. Ménétrier, E. Suard, C. Delmas, *Solid State Ionics* **2000**, *128*, 11.
[62] N. Li, S. Sallis, J. K. Papp, J. Wei, B. D. McCloskey, W. Yang, W. Tong, *ACS Energy Lett.* **2019**, *4*, 2836.
[63] V. Petříček, M. Dušek, L. Palatinus, *Zeitschrift für Kristallographie - Crystalline Materials* **2014**, *229*, 345.
[64] B. Ravel, M. Newville, *J Synchrotron Rad* **2005**, *12*, 537.